Electronic Supporting Information for

Enhancing Electroactive Biofilm Discovery by Combining Microfluidics with a New Integrated Genome Scale and Fluid Dynamics Model

Jiao Zhao[a], Mir Pouyan Zarabadi[b], Derek M. Hall[c], Sanjeev Dahal[a], Jesse Greener*[b] and Laurence Yang*[a]

[a]   Dr. J. Zhao, Dr. S. Dahal, Dr. L. Yang
        Department of Chemical Engineering
        Queen's University
        Kingston, Ontario, Canada, K7L 3N6
        E-mail: laurence.yang@queensu.ca

[b]   Dr. M. Zarabade, Dr. J. Greener
        Department of Chemistry
        Laval University
        Quebec (Quebec), Canada G1V 0A6
        E-mail: Jesse.Greener@chm.ulaval.ca

[c]   Dr. D. Hall
        Department of Energy and Mineral Engineering
        The Pennsylvania State University
        PA 16802, USA

This PDF file includes:

Supporting text

Figures S1 to S11

Tables S1

Legends for Datasets S1 to S5

SI References

Other supporting materials for this manuscript include the following:

Datasets S1 to S5

Supporting Information Text

Technical details about GEM-FRTM (Genome-scale Metabolic Model coupled to Flow and Reactive Transport Model) for EABs (Electrochemically Active Biofilms)

(1) Three methods to describe *Geobacter sulfurreducens* (GS) growth and metabolism in EAB

We used three methods to describe GS growth and cellular metabolism (e.g. acetate uptake rates and GS growth rates) – (1) Michaelis-Menten (MM) kinetics, (2) Flux Balance Analysis (FBA) for GEM, and (3) Surrogate models to replace GEM.

MM kinetics: The first method used the MM kinetics of acetate uptake to describe the overall GS growth and metabolism while treating the bacterial internal workings as a black box (Eq. S1 and Eq. S1).

$$R_{ace} = V_{max,ace} \frac{C_{ace}C_{GS}}{K_M+C_{ace}}$$
Eq. S1

$$R_{GS} = Y_{GS/ace}R_{ace}$$
Eq. S2

where R_{ace} and R_{GS} are the acetate uptake rates (mmol mm^{-3} h^{-1}) and growth rates (g mm^{-3} h^{-1}), respectively, and C_{ace} and C_{GS} are the acetate (mmol mm^{-3}) and biomass concentration (g mm^{-3}), respectively.

Flux Balance Analysis (FBA) for modernized GEM: The second method was based on GEM by applying flux balance analysis (FBA) to the GEM of GS. FBA computes the vector of reaction fluxes (mmol g^{-1} h^{-1}) that maximizes a cellular objective function (i.e., maximization of the specific growth rate, h^{-1}), subject to mass balance constraints at steady-state for reaction network stoichiometry *S* and nutrient uptake rate constraints (Eq. S3). Formally, FBA is formulated as the following linear program.

$$\begin{aligned}
&\text{maximize } f^T V \\
&\text{subject to } SV = 0 \\
&V_l \leq V \leq V_u
\end{aligned}$$
Eq. S3

where V is the vector of n reaction fluxes (mmol g^{-1} h^{-1}), f is the objective function vector, *S* is the stoichiometric matrix for *m* constraints, including the intracellular metabolite mass balance, and *l* and *u* are the lower and upper bounds on metabolic fluxes, respectively. For the acetate uptake reaction with metabolic flux V_{ace}, we additionally constrained its flux via the MM rate equation (Eq. S4). Thus, the acetate uptake flux (Eq. S5) and growth rate (Eq. S6) of GS cells are dependent on the local acetate concentration surrounding the CS cell surfaces, representing the local metabolic status.

$$V_{ace} \leq V_{u,ace} = \frac{V_{max}C_{ace}}{K_M+C_{ace}}$$
Eq. S4

$$R_{ace} = V_{ace}C_{GS}$$
Eq. S5

$$R_{GS} = V_{GS}C_{GS}$$
Eq. S6

A modernized GS GEM has updated GEM for GS (GS_v2) [1] based on the original GS_v1 [2]. First, any orphan metabolites and their associated reactions were removed from the model. Second, mass and charge balancing were performed by adding the metabolite information from the BiGG (Biochemical Genetic and Genomic) [3] database. If information about a metabolite could not be found, the relevant formula and charge were derived by mass and charge balancing of the reactions with which they are associated. For cytochromes, due to the absence of concrete knowledge, the formula and charge of the metabolites that were most extensively annotated in the BiGG database were used. Third, any erroneous names for the gene–protein-reaction (GPR) association were removed from its respective reaction, which was assigned an empty string for unknown GPR association instead of the reaction names. Finally, the updated GEM was converted to human-readable BiGG format [4].

The modernized GS GEM structure is outlined in GS_v3.xlsx in Dataset S1. The new GEM of a GS cell (GS_v3) consists of 466 metabolites, 538 reactions, 889 genes and 367 reactions with gene–protein-reaction association. The improved GS GEM is provided in EXCEL (Dataset S1), SBML (Dataset S2), and MATLAB MAT (Dataset S3) format.

Quality assessment was performed for the modernized GS GEM version (GS_v3) by the open-source Python-based metabolic model testing tool (MOMOTE) [5]. The quality report is shown in Figure S1. MOMOTE reported 100% consistency in stoichiometry, mass balance, charge balance and metabolite connectivity.
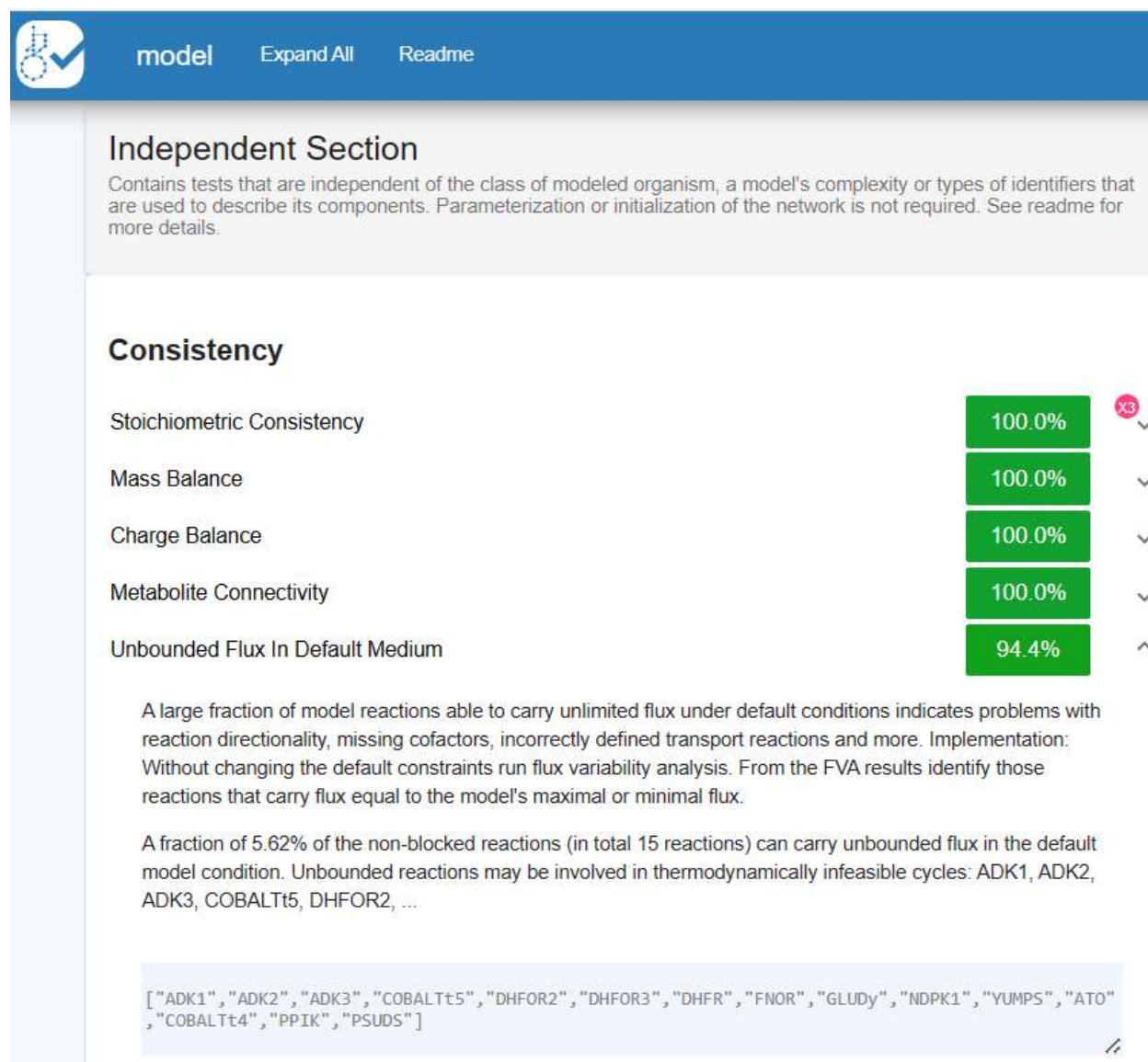

Independent Section

Contains tests that are independent of the class of modeled organism, a model's complexity or types of identifiers that are used to describe its components. Parameterization or initialization of the network is not required. See readme for more details.

Consistency

Stoichiometric Consistency	100.0%
Mass Balance	100.0%
Charge Balance	100.0%
Metabolite Connectivity	100.0%
Unbounded Flux In Default Medium	94.4%

A large fraction of model reactions able to carry unlimited flux under default conditions indicates problems with reaction directionality, missing cofactors, incorrectly defined transport reactions and more. Implementation: Without changing the default constraints run flux variability analysis. From the FVA results identify those reactions that carry flux equal to the model's maximal or minimal flux.

A fraction of 5.62% of the non-blocked reactions (in total 15 reactions) can carry unbounded flux in the default model condition. Unbounded reactions may be involved in thermodynamically infeasible cycles: ADK1, ADK2, ADK3, COBALTt5, DHFOR2, ...

["ADK1","ADK2","ADK3","COBALTt5","DHFOR2","DHFOR3","DHFR","FNOR","GLUDy","NDPK1","YUMPS","ATO","COBALTt4","PPIK","PSUDS"]

Fig. S1. Quality assessment of GS GEM model (GS_v3) by MOMOTE

MOMOTE identified 5.62% (15 reactions) of the reactions that may carry unbounded metabolic fluxes, which are involved in thermodynamically infeasible loops. The Loopless-FBA approach [6] implemented by mixed-integer linear programming (MILP) algorithm was used to eliminate these thermodynamically infeasible loops found in FBA. The results were compared with those obtained by the AllowLoops-FBA

approach [6] by linear programming (LP) algorithm. It was found that the 15 unbounded metabolic fluxes estimated by the AllowLoops-FBA had no effect on the GS phenotypes represented by extracellular metabolic fluxes (Fig. S2 for Loopless-FBA and Fig. S3 for LoopAllowed-FBA).
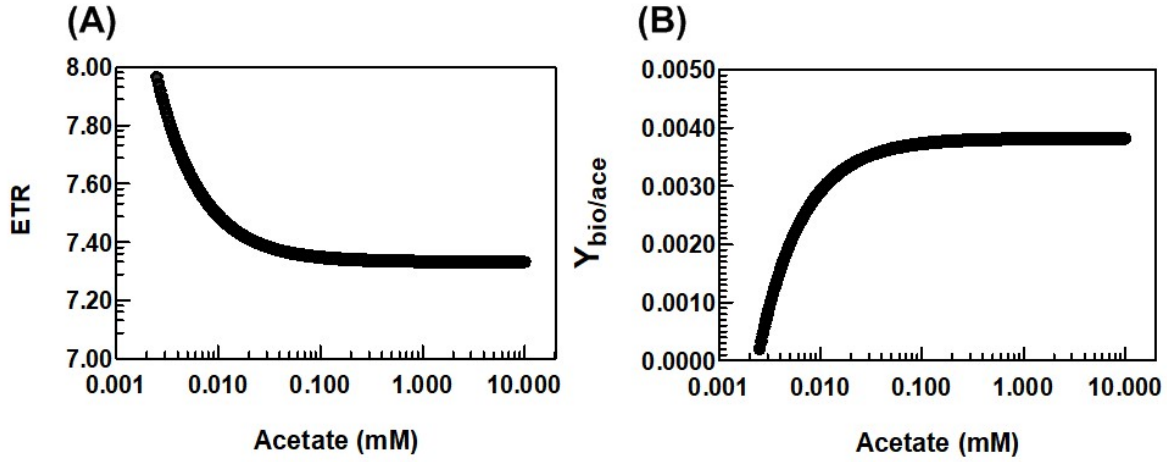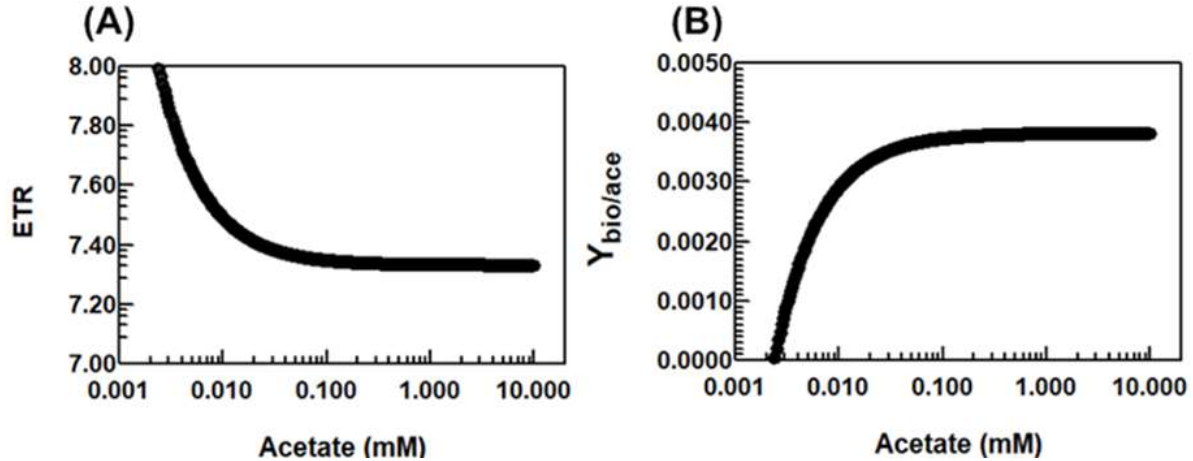
(A)

(B)

Fig. S2. Loopless FBA approach: (A) Semi-log regression of GEM-predicted electron transfer ratio (ETR, number of electrons transferred to current per oxidized acetate molecule) as a function of local acetate concentration; (B) semi-log regression of GEM-predicted biomass yield ($Y_{bio/ace}$, g dry-cell-weight biomass produced per mmol of acetate oxidized) as a function of local acetate concentration.

(A)

(B)

Fig. S3. AllowLoops FBA approach: (A) Semi-log regression of GEM-predicted electron transfer ratio (ETR, number of electrons transferred to current per oxidized acetate molecule) as a function of local acetate concentration; (B) semi-log regression of GEM-predicted biomass yield ($Y_{bio/ace}$, g dry-cell-weight biomass produced per mmol of acetate oxidized) as a function of local acetate concentration.

Surrogate models to replace GEM: The third method used pre-calculated FBA predictions of the GS GEM model for the 10,000 possible concentrations of acetate ranging from 0.002 to 10 mM at a step size of 0.001 mM. These concentration points are environmentally relevant to those potentially observed in real microfluidics devices with respect to time and space. Next, we performed polynomial regression to obtain the relationship between the independent concentration variable (C_{ace}) on a logarithmic scale and the dependent variable (electron transfer ratio and biomass yield, Eq. S1 and S2) expressed as an nth degree polynomial in C_{ace}. Here, the electron transfer ratio (ETR) is defined as the number of electrons (mmol) transferred to the anode per mmol of acetate oxidized, and the biomass yield ($Y_{bio/ace}$) refers to the grams of dry-cell-weight biomass produced per mmol of acetate consumed. Thus, during execution of the microfluidics model, the polynomial function can be called at each time step and for each grid point to define ETR and $Y_{bio/ace}$ at the given acetate concentrations.

ETR = $0.0020*(\log10(c))^6 + 0.0008*(\log10(c))^5 - 0.0013*(\log10(c))^4 - 0.0055*(\log10(c))^3 + 0.0060*(\log10(c))^2 - 0.0032*(\log10(c))^1 + 7.3340$ \hspace{2em} Eq. S7

$Y_{bio/ace}$ = $-0.000012*(\log10(c))^6 -0.0000049*(\log10(c))^5 +0.0000072*(\log10(c))^4 +0.000032*(\log10(c))^3 - 0.000035*(\log10(c))^2 +0.000018*(\log10(c))^1 +0.0038$ \hspace{2em} Eq. S8

The polynomial function, when coupled to the FRTM, was then called at each time step and each grid point to compute ETR and $Y_{bio/ace}$ in the local extracellular environment. Fig. S4 indicates that such an indirect GEM method (iGEM) can exactly duplicate the GEM method (GEM). In other words, iGEM achieves the best aspects of GEM (accuracy) and MM modeling (speed).
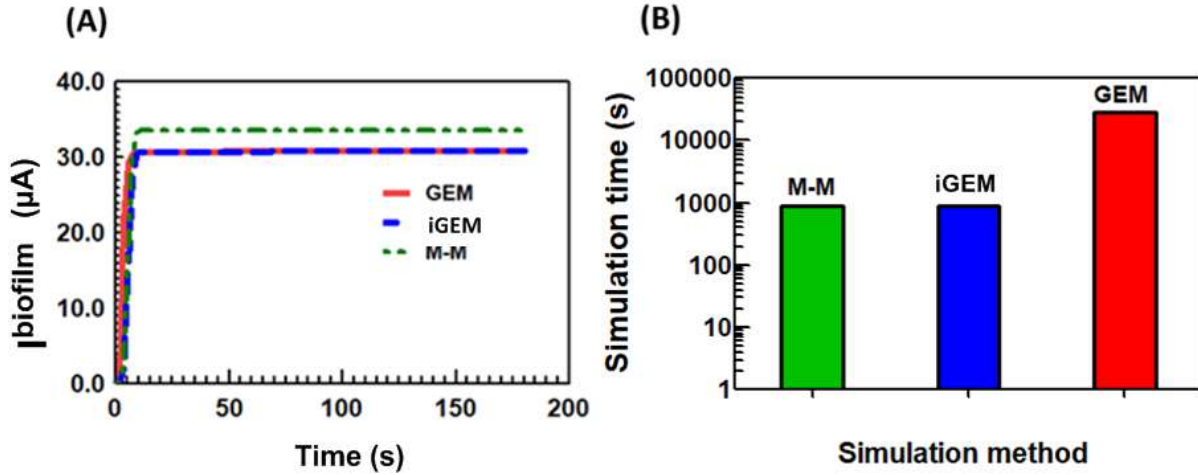
Fig. S4. Performance comparison for three methods (A) Simulated $I^{biofilm}$ from direct Michaelis-Menten (MM, green), indirect GEM coupling algorithm (iGEM, blue), and GEM coupling algorithm (GEM, red) under 8.0 mL h^{-1} flow rate of 10 mM acetate. (B) Computational cost for MM, GEM and iGEM coupling algorithms with same color-coding as in (B).

(2) Background of GEM-FRTM for GS

Among GS modeling approaches, the flow and reactive transport model (FRTM) has been used to predict uranium bioremediation in groundwater via acetate loading [7, 8]. Monod-type growth kinetics were used to represent various multi-enzyme cycles as a general black box in the FRTM, which linked the reduction rates of extracellular electron acceptors (e.g., Fe^{3+} and U^{6+}) to the acetate oxidation rates through universally applied electron-transfer ratios (ETR) and biomass yields ($Y_{bio/ace}$). However, the FRTM model did not account for the reality that spatiotemporal environmental conditions may influence the metabolism of the GS bacteria at different locations within the biofilm. Some work has partially addressed this gap with genome-scale metabolic modeling (GEM), which integrated the GS intracellular metabolic network with the local extracellular environment for bioremediation applications [9]. Their GEM used a metabolic flux balance analysis (FBA) to calculate the optimal reduction rates and biomass production rates from the rates at which acetate oxidation proceeded through intracellular metabolism. Hence, the reaction stoichiometry, yield, and transfer coefficients in that study could vary to reflect the ability of GS cells to respond to their local environment. However the model did not capture the entire 3-dimensional porous structure of a real GS biofilm because the spatial resolution was at the decimeter scale or larger [9], whereas thicknesses of metabolically active biofilms are less than a fraction of a millimeter [10]. Moreover, GEM generally represents the cellular metabolic response to its immediate extracellular environment. To this end, we refer to the "cell-scale" as the scale at which cells interact with their local environment. To reduce this gap in scale, a subsequent example from the literature coupled GEM to FRTM (GEM-FRTM) through the soil pore spaces [11]. However, this simulation was computationally intensive due to the small soil pore dimensions, so the authors had to increase all reaction rates in their model by a factor of 10^3 to speed up the coupling between biotic and abiotic processes. Again, the model did not have sufficient spatial resolution to consider the GS

within the biofilm 3D matrix and therefore could not account for variations in metabolic activities within the biofilm. A recent FRTM paper for another *Geobacter* species (*Geobacter metallireducens* - abbreviated as GM) managed to keep track of moving for all individual cells to describe the dynamical development of growing biofilms in porous media by lattice Boltzmann method [12]. However, the long-term performance of the mature *Geobacter* biofilms for electricity production remains unclear.

A more useful model for BES should consider cell accumulation into electrode-adhered biofilms with thicknesses at an appropriate length scale that can account for internal concentration gradients, effective diffusivity, and advection through the biofilm. It is known that electrode-adhered GS can develop metabolically active biofilms with thicknesses greater than 50 μm [10] and average porosities greater than 0.45 [13]. Reduced diffusional mass transport of acetate ions (CH_3COO^-), the major substrate for GS, in biofilms with thickness greater than 45 μm has been associated with limitations to electrochemical activity [14]. This observation is corroborated by another study that showed a stratification of fluorescent tracers between accessible regions near the biofilm/liquid interface and inaccessible regions deeper in the GS biofilm [15]. One can understand such limitations in diffusion as being caused by acetate confinement in pores and increased molecular adsorption and simultaneous consumption in dense bacterial clusters [16, 17]. The diffusion of negatively charged acetate ions may also be influenced by electrostatic interactions in these confined pore spaces within the GS biofilm [18]. Given that all mass transport inside a biofilm is traditionally attributed to diffusion in the BES literature [13] and that GS biofilm properties vary widely based on age and culture conditions [19], it is no surprise that missing contributions to other mass transport mechanisms has resulted in such a wide range of diffusivities being reported in the literature (0.7–9.0 mm² h⁻¹) [13, 17].

(3) Flow and reactive transport model for GS EABs

The Navier-Stokes-Brinkman equation for CFD (Eq. S9) and the diffusion-advection-reaction equation (Eq. S10 and Eq. S11) for reactive-transport are applied to each discrete point in the biofilm subdomain (SD3 in Fig. 5).

$$\frac{1}{\varphi}\left(\frac{\partial \rho \vec{v}}{\partial t} + \nabla \cdot \left(\frac{\rho}{\varphi}\vec{v}\vec{v}\right)\right) = -\nabla p + \nabla \cdot \frac{\mu}{\varphi}(\nabla\vec{v} + \nabla^T\vec{v}) - \mu k^{-1}\vec{v} \qquad \text{Eq. S9}$$

$$\frac{\partial C_{ace}}{\partial t} + \nabla \cdot (-D_{ace}\nabla C_{ace}) = R_{ace} - \vec{v}\nabla C_{ace} \qquad \text{Eq. S10}$$

$$\frac{\partial C_{GS}}{\partial t} + \nabla \cdot (-D_{GS}\nabla C_{GS}) = R_{GS} - \vec{v}\nabla C_{GS} \qquad \text{Eq. S11}$$

where φ is the porosity, $\vec{v}$ is the flow velocity vector, ρ is the fluid density, p is the static pressure, k is the permeability, D_{ace} and D_{GS} are the diffusion coefficients for acetate and biomass, respectively, μ is the dynamic viscosity, R_{ace} and R_{GS} are local acetate uptake rates and growth rates for GS, and C_{ace} and C_{GS} are local acetate and biomass concentration, respectively. All parameters describe the physical and biological phenomena in local environments (cell-scale), represented by the discrete points in the finite element method, and D_{GS} is set to zero.

The iGEM-FRTM uses the bottom-up approach to calculate $I^{biofilm}$ by adding up the local I^{cell} in all finite-sized geometric shapes defined by the model mesh (e.g., triangles or squares) that are linked by local mass transfer.

$$I^{biofilm} (\mu A) = \sum_{i=1}^{n}(I^{cell}) = \sum_{i=1}^{n}(FI \times ETR \times V_{ace} \times C_{GS} \times \Delta V) \qquad \text{Eq. S12}$$

where n is the number of the discrete points, FI represents the flux to current constant, obtained by $\frac{1\,mmol}{g \cdot h} \cdot \frac{96485C}{mol} = \frac{1\,mol}{1000g \cdot 3600s} \cdot \frac{96485C}{mol} = 0.0268\,\frac{A}{g}$, R_{ace} is the cell-scale acetate uptake rate (mmol mm⁻³ h⁻¹), ΔV is the local volume for a discrete point.

The advection and diffusion fluxes in space and time were predicted by the full microfluidics model, and the overall advection and diffusion fluxes at steady state (i.e., $J_{adv}^{biofilm}$ and $J_{diff}^{biofilm}$) were estimated for each

6

flow condition as the sum of all simulated advection and diffusion fluxes from individual local environment at the cell-scale (i.e., J_{adv}^{cell} and J_{diff}^{cell}) based on the discrete grid points

$$J_{adv}^{biofilm} = \sum_{i=1}^{n}(J_{adv}^{cell}) = \sum_{i=1}^{n}(\vec{v} \times C_{ace}) = \sum_{i=1}^{n}\left(\sqrt{v_x^2 + v_y^2} \times C_{ace}\right) \qquad \text{Eq. S13}$$

$$J_{diff}^{biofilm} = \sum_{i=1}^{n}(J_{diff}^{cell}) = \sum_{i=1}^{n}\left(D \times \sqrt{\left(\frac{dC_{ace}}{dx}\right)^2 + \left(\frac{dC_{ace}}{dy}\right)^2}\right) \qquad \text{Eq. S14}$$

The Péclet number (P_{eL}) was used to evaluate whether advection or diffusion has a significant contribution to the mass transport occurring in the biofilm (Eq. S15, SI Appendix).

$$P_{eL} = \frac{J_{adv}^{biofilm}}{J_{diff}^{biofilm}} \qquad \text{Eq. S15}$$

The full microfluidics model (GEM-FRTM) was built in FEATool Multiphysics (https://www.featool.com/) version 1.15 for Matlab. The Featool model for the full microfluidics device and the model structure readable by Matlab are provided in Dataset S4 and S5 (GS_microfluidics_model.fea and GS_microfluidics.mat).

(4) Parameters in GEM-FRTM for GS EABs (mass transport and kinetics)

With iGEM coupled to FRTM (iGEM-FRTM) in hand, we sought to iteratively tune the model parameters starting with experimentally determined values found in the literature and reasonable estimates. The simulation parameters included the local mass transport values in local environments (i.e., the cell-scale), namely, diffusion (D, mm^2 h^{-1}), permeability (k, mm^2), and porosity (φ, unitless), and the biological kinetic parameters at a cell-scale, namely, the maximum cellular reaction rate at saturating concentration (V_{max}^{cell}, mmol g^{-1} h^{-1}), the cellular half-maximum rate concentration (otherwise known as the MM constant, K_M^{cell}, mmol mm^{-3}), and the initial acetate-accessible catalytic biomass concentration (BMC, g mm^{-3}).

Among these parameters, BMC is hard to measure within EAB, and correct estimation of D and k can be affected in the presence of interference, such as flow through EAB, frustrated movement through tortuous paths [20], diffusion barrier around cells [21], molecular adsorption [22], and ion-biofilm coulombic interactions [18].

BMC estimation: BMC was based on biofilm geometry and bacterial cell properties:

Volume of biofilm above the working electrode (WE):
XYZ =3000 μm × 2000 μm × 80 μm = 4.8e+08 μm^3

Volume of a bacterium (average):
π × r^2 (radius of bacteria) × h (length of bacteria) =3.14 × (0.25 μm)^2 × (1.7 μm) = 0.33 μm^3

Number of total cells in the test biofilm:
4.8e+08/0.33= 1.45e+09

0.12–0.33 g dry weight per cubic centimeter of cell volume [23]
average = 0.2250

Dry cell weight per cell
0.33*1e-09*0.2250/1e+03 = 7.4250e-14 g

Total biomass weight
7.4250e-14*1.45e+09

Active biomass concentration (BMC)

7.4250e-14*1.45e+09/(4.8e+08*1e-09) = 224e-06 g mm^{-3}

BMC upper bound
Adjust by average porosity 0.47: 0.53*224e-06 = 120e-06 g mm^{-3}

BMC lower bound
50% EPS and proteins: 120e-06*0.5 = 60e-06 g mm^{-3}

BMC range
[60e-06, 120e-06] g mm^{-3} = [60, 120] g L^{-1}

Diffusion coefficient (D): Mass transport in this study has been decoupled by advection and diffusion. The diffusion coefficient (D) for acetate in the GS biofilm was initially set from 0.05 to 0.10 mm^2 h^{-1}, lower than the reported values in the literature (e.g. 0.7 ~ 9.0 mm^2 h^{-1}) [13]. Mathematically, A smaller D than the reported values ignoring the advection inside a biofilm is consistent with both advection and diffusion contributing to the mass transport of acetate. This was confirmed under both our and reported experimental conditions (i.e., higher acetate concentration at 1 mL h^{-1} of flow) [13] where advection was omitted inside the biofilm.

Flow-insensitivity (Fig. S5) under low flow rates between 0.4 and 2.0 mL h^{-1} at high acetate concentrations was found when a wide range of D from 0.05 to 5.0 mm^2 h^{-1} was used and diffusion was considered as the only mass transport process inside our GS biofilm. This is contrary to what has been observed experimentally at these flow rates (red lines), where the total experimental current (I^{exp}) was found to increase with flow rates at high acetate levels ranging from 7 mM to 10 mM. Thus, it supports the presence of flow inside EAB, which was often ignored in BES studies.
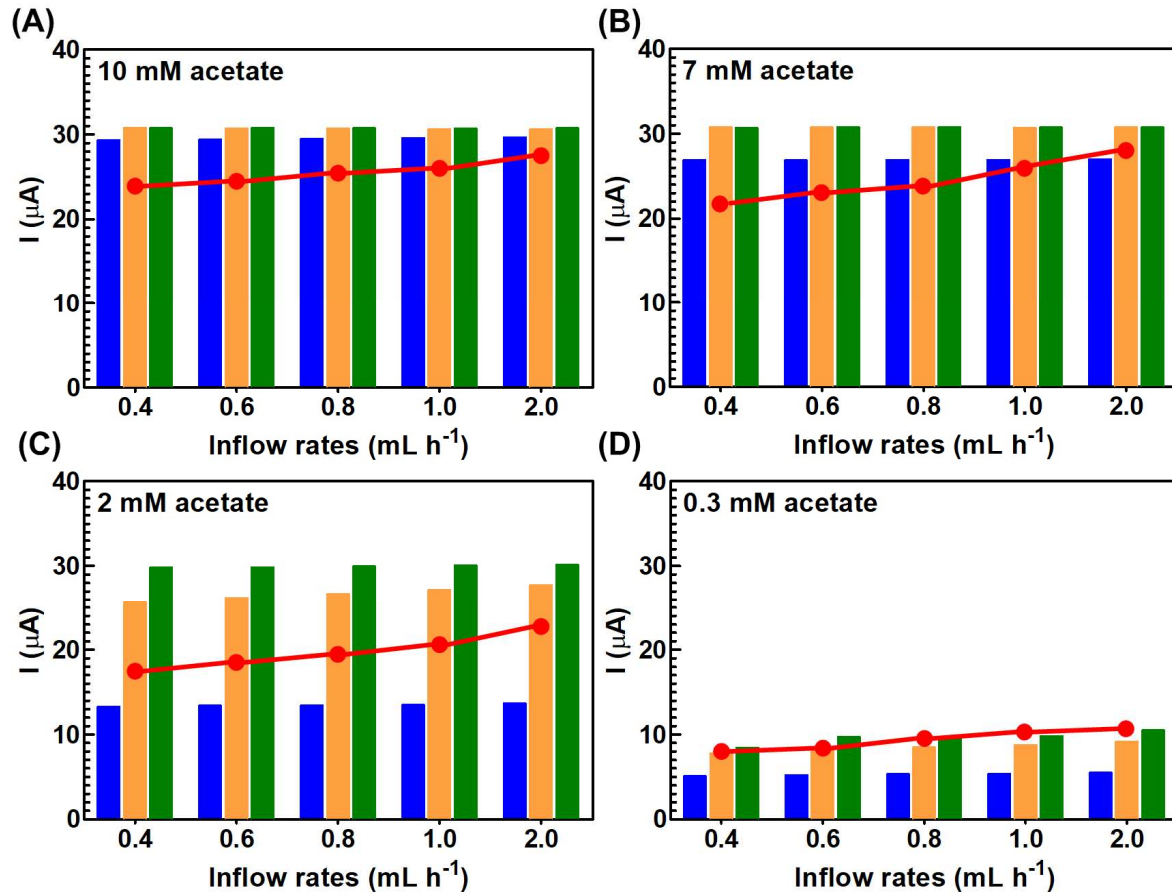

Fig. S5. The sensitivity of biofilm-scale currents simulated ($I^{biofilm}$, bars) and measured (I^{exp}, red dots) to flow rates when diffusion is the only mass transport process inside the GS biofilm while flow only modulates the boundary layers around the biofilm when passing

8

through other compartments. $I^{biofilm}$ simulated at local D: ■ 0.05 mm² h⁻¹; ■ 0.50 mm² h⁻¹; ■ 5.0 (mm² h⁻¹); ● measured I^{exp} from microfluidic experiments. Inflow acetate concentrations: (A) 10 mM and (B) 7.0 mM, (C) 2.0 mM, and (D) 0.3 mM.

Fig. S6 further indicates that the diffusion-driven-only D has to be increased in GEM-FRTM to reach the $I^{biofilm}$ level obtained by both diffusion and advection contribution under reported experimental conditions.
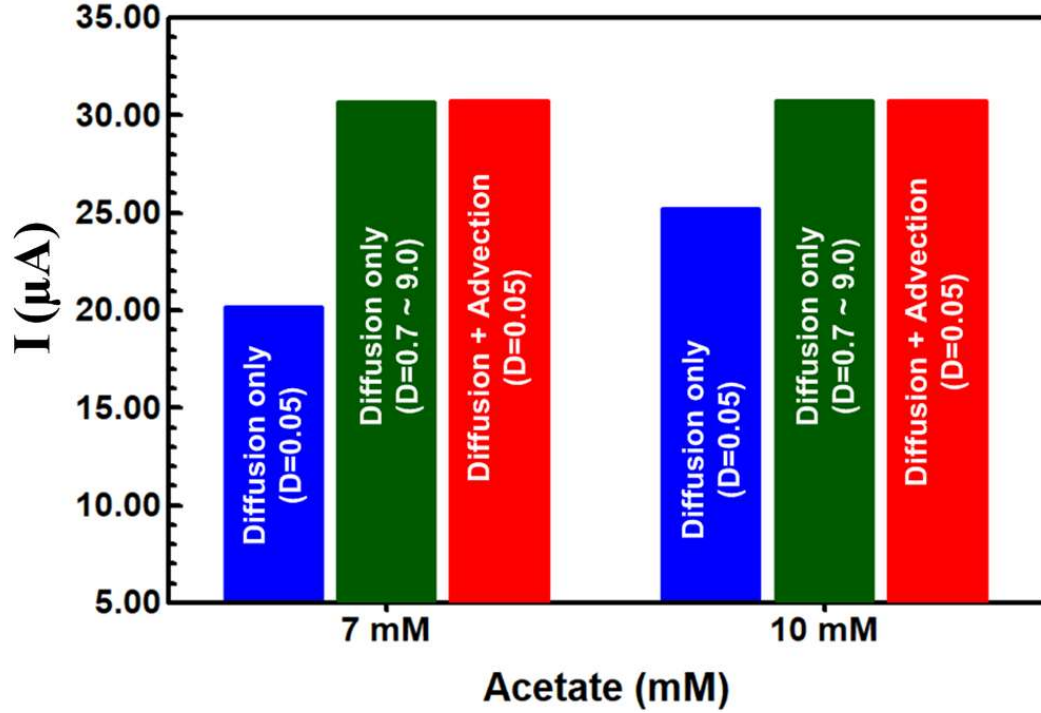

Fig. S6. $I^{biofilm}$ estimated by iGEM-FRTM with diffusion-driven-only and diffusion-advection simulations. Under reported experimental conditions (higher acetate concentration at 1 mL h⁻¹ of flow) where advection was omitted inside the biofilm, the diffusion-driven-only D has to be increased in iGEM-FRTM to reach the $I^{biofilm}$ level obtained by both diffusion and advection contribution.

Permeability (k): There is little information about the magnitude of k inside an EAB. The k in a biofilm-porous medium system was reported to range from 10^{-9} to 10^{-1} mm².[24] Considering that the k values were estimated for porous medium systems, their magnitudes may not reflect the reality in the biofilm system alone. Moreover, the test biofilms (e.g., B. subtilis) are rich in extracellular biopolymers such as extracellular polymeric substances (EPS), DNA and proteins [25], which are different from the GS biofilm characteristics. Thus, we used our GEM-FRTM model simulations to preliminary determine the range of k from 2×10^{-4} to 2×10^{-3} mm² based on the experimental data of I^{exp} across a wide range of inflow acetate rates and concentrations (see Figure 1 red band). This k range was consistent in magnitude with that used in a published FRTM for a general bacteria system [26]. Furthermore, the GEM-FRTM indicates that once k was further decreased beyond the lower bound at 2×10^{-4} mm², the simulation cannot reproduce the stable I^{exp} at 10 mM inflow acetate concentration after 0.07 hours but significantly decreasing $I^{biofilm}$ to zero, suggesting the numerical issue due to the low input k values causing the incorrect mass transport performance for the GS biofilm system.

(5) Biofilm structure

Biofilm structures are subject to reversible change with flow and substrate concentrations [27-29]. To reflect the loose structure of the GS biofilm under low flow rates and acetate concentrations, D and k upper bounds were extended to 0.30 mm² h⁻¹ and 2.5×10^{-3} mm², respectively, to refine the mass transport parameters based on mechanical properties of the GS biofilm under these circumstances. We obtained a best match between $I^{biofilm}$ and I^{exp} by using the profiles of φ, D and k shown in Fig. S7.

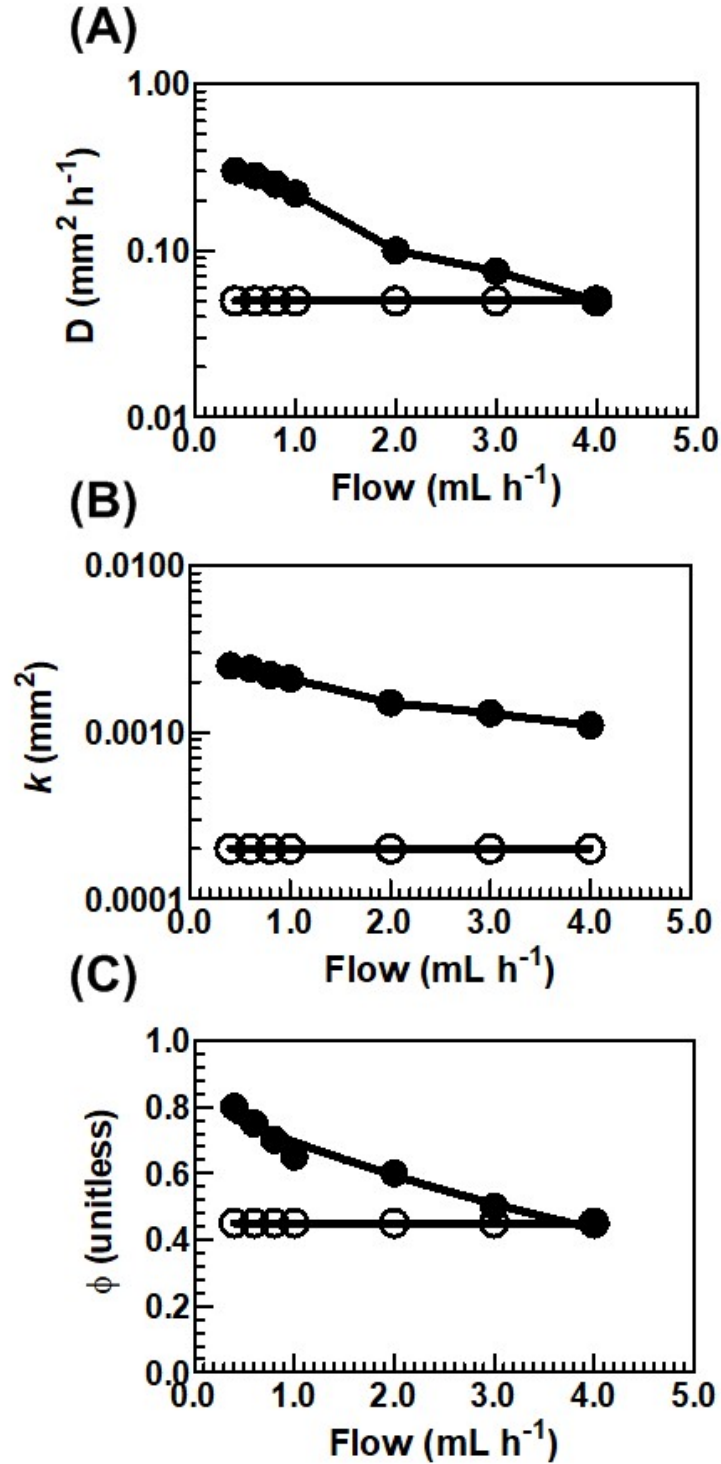Fig. S7. (A) The profiles of φ, D and k when a best match between I^{biofilm} and I^{exp} (Figure 3) was obtained. Solid circle (0.3 mM acetate); open circle (10 mM acetate). (A) diffusion vs. flow rates; (B) permeability vs. flow rates; (C) porosity vs. flow rates

Homogeneous vs. heterogeneous biofilm: An extended version of the iGEM-FRTM was developed to deal with EAB heterogeneities as a function of the x- and y-coordinates in 2D (Fig. S8). The simulations suggest that the biofilm spatial structures may have a significant effect on the electricity generation (Fig.

S8), fluid dynamics and concentration gradients (Fig. S9). Therefore, they cannot be simplified as spatial-independent parameters in large-scale biofilm bioreactors.
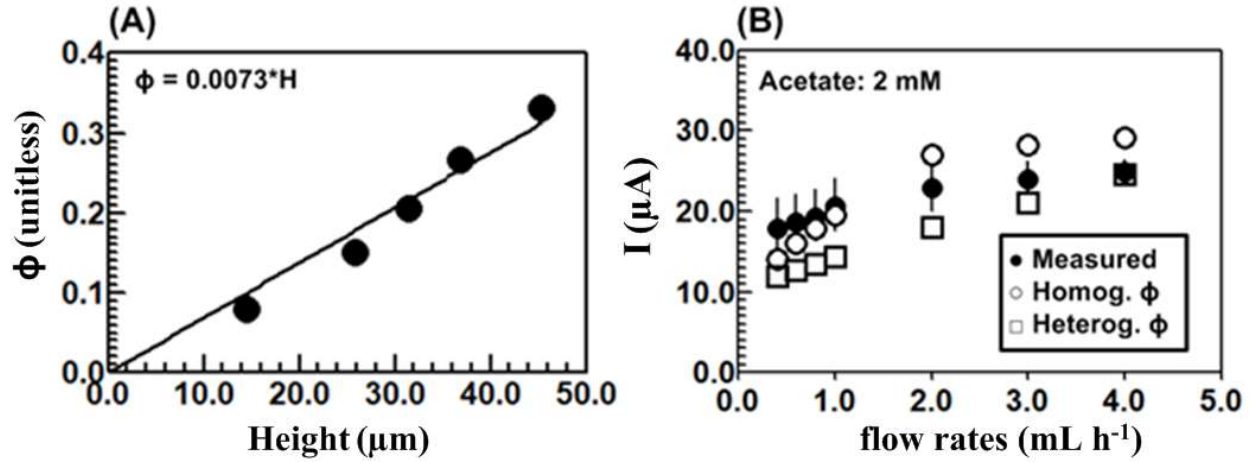

Fig. S8. Model extension: effect of biofilm structure heterogeneity (porosity) on the electricity production. (A) porosity represented as an empirical function of the biofilm height based on flow reactor experimental data; (B) I (µA) vs flow rates under different biofilm structure

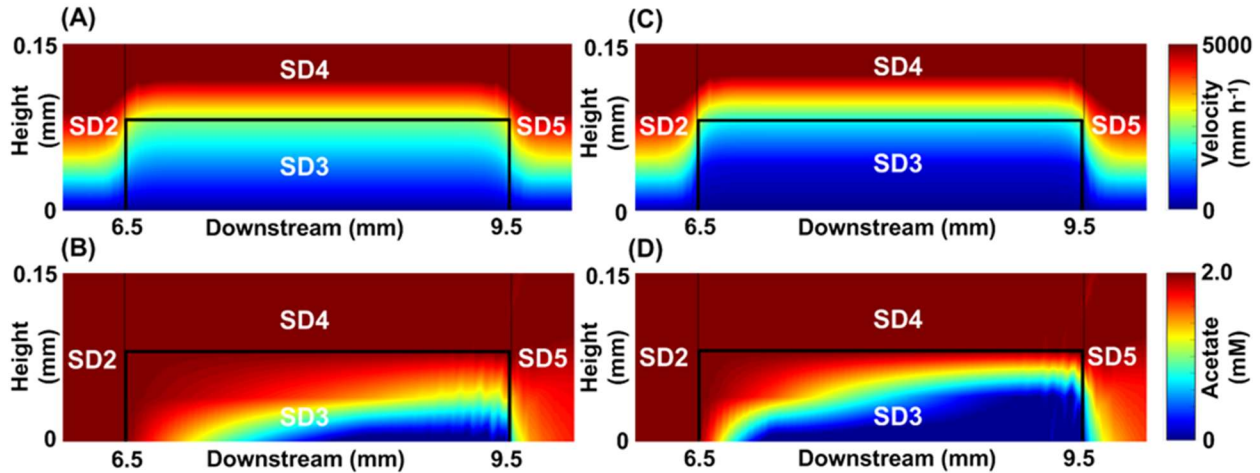Fig. S9. Homogeneous biofilm (constant φ) (A) flow field at flow rates of 4.0 mL h^{-1} (B) acetate concentration map at flow concentration of 2.0 mM Heterogeneous biofilm (φ as a function of a biofilm height; φ = 7.3*H(mm) based on experimental data reported for a ~ 400 µm thick GS biofilm): (C) flow field at flow rates of 4.0 mL h^{-1} (D) acetate concentration map at flow concentration of 2.0 mM

Loose vs. compact biofilm: The iGEM-FRTM provides subtle details about the acetate, active biomass, and flow distribution over the biofilm in response to the culture conditions, which is hard to experimentally characterize. Fig. S10 illustrates the flow and concentration profiles through the modeled GS biofilm, which demonstrate that more of a loosely packed biofilm (high values of φ, k and D) can support faster advective flow than a compacted biofilm (low values of φ, k and D), resulting in different concentration gradients and flow patterns inside and outside the loose biofilm from the compact biofilm.
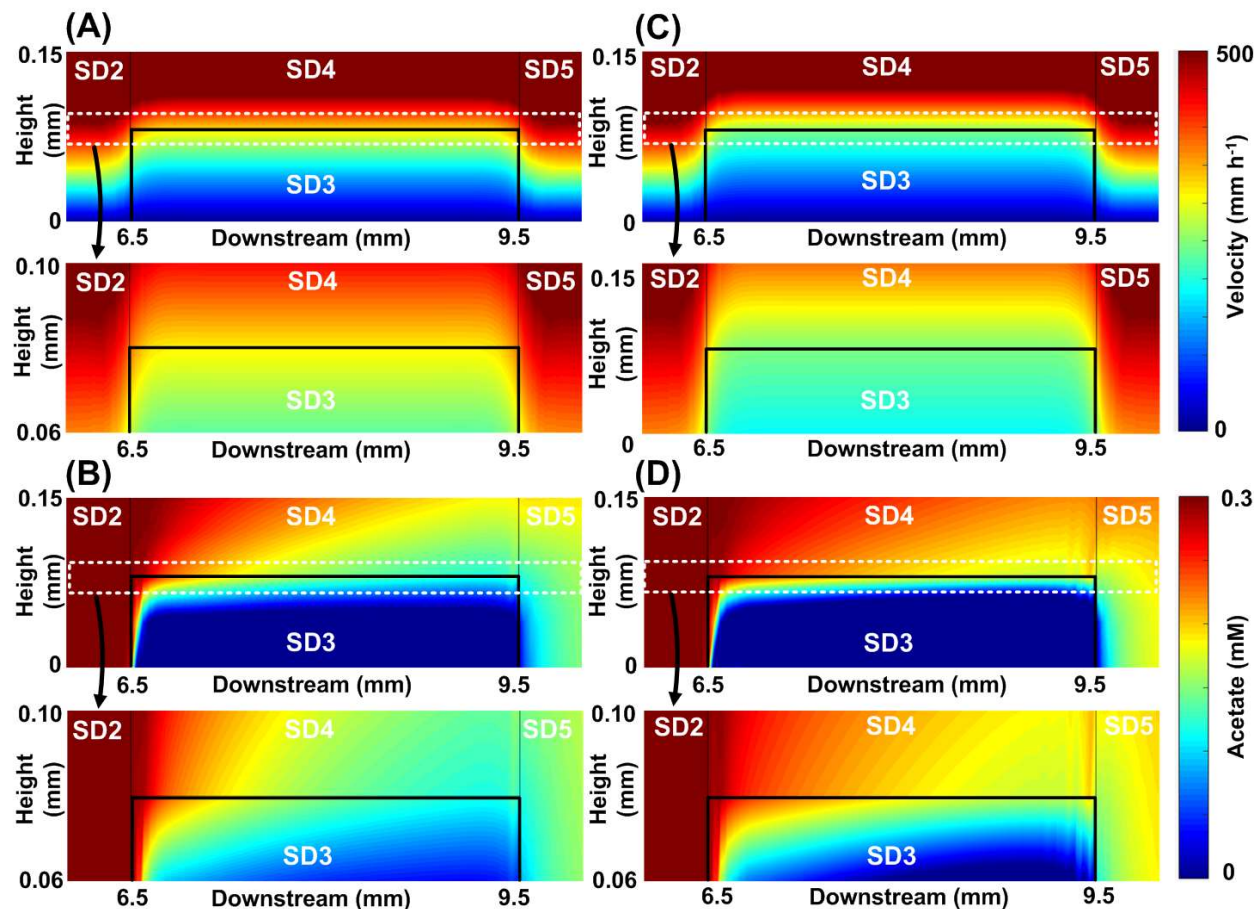
Fig. S10. Different concentration gradients and flow patterns between the loose and compact biofilm. Loose biofilm (A) and (B) (D=0.30 mm^2 h^{-1}, φ=0.80): (A) top sub-figure (flow field from 0 to 150 µm height at inflow rates of 0.4 mL h^{-1}); bottom sub-figure: (zoomed view of the flow field from 60 to 100 µm height at flow rates of 0.4 mL h^{-1}) (B) top sub-figure (acetate concentration map from 0 to 150 µm height at flow concentration of 0.3 mM; bottom sub-figure (zoomed view of the acetate map from 60 to 100 µm height at flow concentration of 0.3 mM) Compact biofilm (C) and (D) (D=0.05 mm^2 h^{-1}, φ=0.45): (C) see (A) captions; (D) see (B) captions. SD2 and SD5: biofilm-free compartments; SD3: biofilm; SD4: headspace over the biofilm. See full subdomains (SD) in Figure 5.

Technical details about Microfluidics device for EAB

We propose microfluidic BES as the best experimental platform for probing advection through the GS biofilm due to the limited ability for flow redirection around it. This couples well with several other advantages of microfluidic experimental platforms in studying biofilms and offers benefits from real-time measurements while exercising precise control over experimental conditions (e.g., hydrodynamics and applied concentrations) [30-32]. As such, microfluidic bioelectrochemical devices have led to a better fundamental understanding of the coupled physical and biological processes in BES [33], especially when combined with numerical models and theory that can account for kinetic and mass transport in and around the biofilm [30, 34-36].

Microfluidics device setup: The microfluidic device for EAB is illustrated in Fig. S11. The gold pseudo-RE was placed upstream to ensure that the conditions were constant during the long-duration growth culture and bioelectrochemical experiments. The final device is the same as used in previous published works. Extensive tests were conducted previously into the stability of a microfluidic device with the same pseudo-RE and its positioning, which validated that the reference voltage was constant throughout the experiment (+400 mV vs. Ag/AgCl with 3 M KCl). Cleaning and sterilization of the channel with a 70% ethanol solution and of the electrodes with 1 M HCl were performed before sealing. The microfluidic

electrochemical cell was sealed with a microscope slide by exposure to air plasma (PCD-001Harrick Plasma, Ithaca, NY, USA). Because the microfluidic device was fabricated in PDMS, which is known to be porous to small molecules, including O_2, an anaerobic enclosure (McIntosh and Filde's, 28029 Sigma-Aldrich) was filled with anaerobic gas (20% CO_2 and 80% N_2) as done previously. The device was placed in the enclosure, and sterile perfluoroalkoxy connective tubing (PFA tube 1/16, Hamilton Inc., Canada) and electrical connections were attached via airtight feedthroughs in the enclosure cap. To minimize air diffusion through the connective tubing outside of the enclosure, a layer of gas-impermeable tape (Loctite 249 Anaerobic Blue Threadlocker Tape, Medium Strength, Henkel Corp., Mississauga, Canada) was applied to the tubing, which was subsequently covered by epoxy glue. The electrical leads were fixed to the graphite WE and CE via alligator clips, and the gold RE was connected by solder with a protective coating of epoxy to physically stabilize the connection. The inlet tube was connected to a 50 mL glass syringe via connector assemblies (P-200x, P-658, IDEX, WA, USA). Syringe pumps (PHD 2000, Harvard Apparatus, Holliston, MA, USA) were used in controlled liquid injection. Before inoculation, the microfluidic channel and tubing were rinsed with sterile distilled water for 1 h at 1 mL h^{-1}.
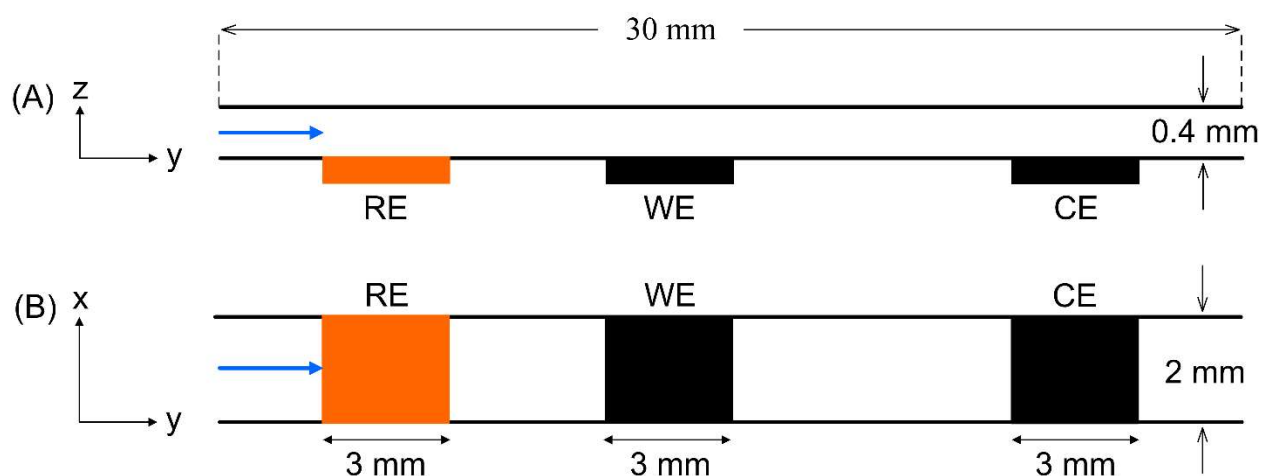

Fig. S11. Schematic of a microfluidic channel from (A) the side view (z-y plane) and (B) the top view (x-y plane). Channel and electrode dimensions are given. Dimensions and electrode spacing are not to scale.

Dataset S1 (separate file). Modernized GS GEM provided in EXCEL format.
Dataset S2 (separate file). Modernized GS GEM provided in SBML format.
Dataset S3 (separate file). Modernized GS GEM provided in MAT format.
Dataset S4 (separate file). Microfluidics full model for GS biofilm in Featool fea format
Dataset S5 (separate file). Microfluidics device structure in MAT format

SI References

[1] K. Zhuang, M. Izallalen, P. Mouser, H. Richter, C. Risso, R. Mahadevan, D. R. Lovley *ISME J*. **2011**, *5*, 305-316.
[2] R. Mahadevan, D. R. Bond, J. E. Butler, A. Esteve-Nunez, M. V. Coppi, B. O. Palsson, C. H. Schilling, D. R. Lovley *Applied and Environmental Microbiology*. **2006**, *72*, 1558-1568.
[3] C. J. Norsigian, N. Pusarla, J. L. McConn, J. T. Yurkovich, A. Drager, B. O. Palsson, Z. King *Nucleic Acids Res*. **2020**, *48*, D402-D406.
[4] Z. A. King, J. Lu, A. Drager, P. Miller, S. Federowicz, J. A. Lerman, A. Ebrahim, B. O. Palsson, N. E. Lewis *Nucleic Acids Res*. **2016**, *44*, D515-522.
[5] C. Lieven, M. E. Beber, B. G. Olivier, F. T. Bergmann, M. Ataman, P. Babaei, J. A. Bartell, L. M. Blank, S. Chauhan, K. Correia, C. Diener, A. Drager, B. E. Ebert, J. N. Edirisinghe, J. P. Faria, A. M. Feist, G. Fengos, R. M. T. Fleming, B. Garcia-Jimenez, V. Hatzimanikatis, W. van Helvoirt, C. S. Henry, H. Hermjakob, M. J. Herrgard, A. Kaafarani, H. U. Kim, Z. King, S. Klamt, E. Klipp, J. J. Koehorst, M. Konig, M. Lakshmanan, D. Y. Lee, S. Y. Lee, S. J. Lee, N. E. Lewis, F. L. Liu, H. W. Ma, D. Machado, R. Mahadevan, P. Maia, A. Mardinoglu, G. L. Medlock, J. M. Monk, J. Nielsen, L. K. Nielsen, J. Nogales, I. Nookaew, B. O. Palsson, J. A. Papin, K. R. Patil, M. Poolman, N. D. Price, O. Resendis-Antonio, A. Richelle, I. Rocha, B. J. Sanchez, P. J. Schaap, R. M. S. Sheriff, S. Shoaie, N. Sonnenschein, B. Teusink, P. Vilaca, J. O. Vik, J. A. H. Wodke, J. C. Xavier, Q. Q. Yuan, M. Zakhartsev, C. Zhang *Nature Biotechnology*. **2020**, *38*, 272-276.
[6] J. Schellenberger, N. E. Lewis, B. O. Palsson *Biophys J*. **2011**, *100*, 544-553.
[7] S. B. Yabusaki, S. S. Sengor, Y. L. Fang *Computational Geosciences*. **2015**, *19*, 551-567.
[8] J. Zhao, T. D. Scheibe, R. Mahadevan *Biotechnology and Bioengineering*. **2011**, *108*, 1537-1548.
[9] T. D. Scheibe, R. Mahadevan, Y. L. Fang, S. Garg, P. E. Long, D. R. Lovley *Microbial Biotechnology*. **2009**, *2*, 274-286.
[10] F. J. Otero, G. L. Chadwick, M. D. Yates, R. L. Mickol, S. H. Saunders, S. M. Glaven, J. A. Gralnick, D. K. Newman, L. M. Tender, V. J. Orphan, D. R. Bond *Applied and Environmental Microbiology*. **2021**, *87*.
[11] G. D. Tartakovsky, A. M. Tartakovsky, T. D. Scheibe, Y. Fang, R. Mahadevan, D. R. Lovley *Advances in Water Resources*. **2013**, *59*, 256-270.
[12] H. Jung, H. S. Song, C. Meile *Geoscientific Model Development*. **2023**, *16*, 1683-1696.
[13] R. S. Renslow, J. T. Babauta, A. C. Dohnalkova, M. I. Boyanov, K. M. Kemner, P. D. Majors, J. K. Fredrickson, H. Beyenal *Energy & Environmental Science*. **2013**, *6*, 1827-1836.
[14] J. Greenman, I. Gajda, J. You, B. A. Mendis, O. Obata, G. Pasternak, I. Ieropoulos *Biofilm*. **2021**, *3*.
[15] L. J. Ren, S. R. McCuskey, A. Moreland, G. C. Bazan, T. Q. Nguyen *Biosensors & Bioelectronics*. **2019**, *144*.
[16] K. C. Quan, J. P. Hou, Z. X. Zhang, Y. J. Ren, B. W. Peterson, H. C. Flemming, C. Mayer, H. J. Busscher, H. C. van der Mei *Critical Reviews in Microbiology*. **2022**, *48*, 283-302.
[17] P. S. Stewart *J Bacteriol*. **2003**, *185*, 1485-1491.
[18] T. Stylianopoulos, M. Z. Poh, N. Insin, M. G. Bawendi, D. Fukumura, L. L. Munn, R. K. Jain *Biophys J*. **2010**, *99*, 1342-1349.
[19] C. M. Khodaparastasgarabad N, Greener J. *ChemRxiv*. **2023**.
[20] J. J. Birmingham, N. P. Hughes, R. Treloar *Philosophical Transactions of the Royal Society of London Series B-Biological Sciences*. **1995**, *350*, 325-343.

[21] P. S. Stewart *Biotechnology and Bioengineering*. **1998**, *59*, 261-272.

[22] M. Vogt, H. C. Flemming, W. S. Veeman *J Biotechnol*. **2000**, *77*, 137-146.

[23] L. R. Bakken, R. A. Olsen *Applied and Environmental Microbiology*. **1983**, *45*, 1188-1195.

[24] D. L. Kurz, E. Secchi, R. Stocker, J. Jimenez-Martinez *Environ Sci Technol*. **2023**, *57*, 5666-5677.

[25] S. Liu, J. Huang, C. Zhang, L. Wang, C. Fan, C. Zhong *Synth Syst Biotechnol*. **2022**, *7*, 965-971.

[26] C. Shin, A. Alhammali, L. Bigler, N. Vohra, M. Peszynska *Mathematical Biosciences and Engineering*. **2021**, *18*, 2097-2149.

[27] H. Beyenal, Z. Lewandowski *Biotechnology Progress*. **2002**, *18*, 55-61.

[28] P. Stoodley, D. deBeer, H. M. Lappin-Scott *Antimicrob Agents Chemother*. **1997**, *41*, 1876-1879.

[29] T. Cherifi, M. Jacques, S. Quessy, P. Fravalo *Frontiers in Microbiology*. **2017**, *8*.

[30] S. Karimifard, X. Li, C. Elowsky, Y. Li *Water Res*. **2021**, *188*, 116536.

[31] H. Straub, L. Eberl, M. Zinn, R. M. Rossi, K. Maniura-Weber, Q. Ren *J Nanobiotechnology*. **2020**, *18*, 166.

[32] M. Pousti, M. P. Zarabadi, M. A. Amirdehi, F. Paquet-Mercier, J. Greener *Analyst*. **2019**, *144*, 68-86.

[33] M. P. Zarabadi, S. J. Charette, J. Greener *Sustainable Energy & Fuels*. **2019**, *3*, 2211-2217.

[34] T. C. Ouyang, X. Y. Hu, W. J. Liu, X. M. Shi, J. Lu *Journal of Power Sources*. **2022**, *521*.

[35] M. P. Zarabadi, M. Couture, S. J. Charette, J. Greener *Chemelectrochem*. **2019**, *6*, 2715-2718.

[36] L. L. Gong, N. Khodaparastsgarabad, D. M. Hall, J. Greener *Electrochimica Acta*. **2022**, *431*.